An electrochemically stable homogeneous glassy electrolyte formed at room temperature for all-solid-state sodium batteries

Xiaowei Chi^{1,2‡}, Ye Zhang^{1‡}, Fang Hao^{1‡}, Steven Kmiec^{3‡}, Hui Dong¹, Rong Xu⁴, Kejie Zhao⁴, Qing Ai⁵, Tanguy Terlier⁶, Liang Wang^{7†}, Lihong Zhao¹, Liqun Guo¹, Jun Lou⁵, Huolin Xin⁸, Steve W. Martin^{3*}, Yan Yao^{1*}

¹Department of Electrical and Computer Engineering and Texas Center for Superconductivity at the University of Houston, University of Houston, Houston, TX, 77204, USA

²Shanghai Institute of Ceramics, Chinese Academy of Sciences, Shanghai 200050, China

³Department of Materials Science & Engineering, Iowa State University, Ames, IA 50011, USA

⁴School of Mechanical Engineering, Purdue University, West Lafayette, IN 47907, USA

⁵Department of NanoEngineering, Rice University, Houston, TX 77005, USA

⁶Shared Equipment Authority, SIMS laboratory, Rice University, Houston, TX 77005, USA

⁷Department of Physics, Northern Illinois University, Dekalb, IL 60115, USA

⁸Department of Physics and Astronomy, University of California, Irvine, Irvine, CA 92697, USA ‡ X. C., Y. Z., F. H., S. K. contribute equally to this work.

[†] Current address: Institute of Advanced Structure Technology and School of Materials Science and Engineering, Beijing Institute of Technology, Beijing 100081, China

^{*} Email: <u>yyao4@uh.edu</u> (Y.Y.) <u>swmartin@iastate.edu</u> (S.M.)

Abstract

All-solid-state sodium batteries (ASSSBs) are promising candidates for grid-scale energy storage. However, there are no commercialized ASSSBs yet, in part due to the lack of a low-cost, simple-to-fabricate solid electrolyte (SE) with electrochemical stability towards Na metal. In this work, we report a family of oxysulfide glass SEs (Na₃PS_{4-x}O_x, where $0 < x \le 0.60$) that not only exhibit the highest critical current density among all Na-ion conducting sulfide-based SEs, but also enable high-performance ambient-temperature sodium-sulfur batteries. By forming bridging oxygen units, the Na₃PS_{4-x}O_x SEs undergo pressure-induced sintering at room temperature, resulting in a fully homogeneous glass structure with robust mechanical properties. Furthermore, the self-passivating solid electrolyte interphase at the Na|SE interface is critical for interface stabilization and reversible Na plating and stripping. The new structural and compositional design strategies presented here provide a new paradigm in the development of safe, low-cost, energy-dense, and long-lifetime ASSSBs.

Low-cost batteries with high safety and specific energy are in ever-increasing demand for grid-scale energy storage¹. All-solid-state sodium batteries (ASSSBs) using nonflammable solidstate electrolytes (SEs) and earth-abundant sodium metal anodes are among the most promising candidates and therefore are attracting worldwide research attention²⁻⁵. So far, the only successful example of a commercialized Na metal anode battery for grid-scale energy storage is the wellknown high-temperature sodium-sulfur battery⁶. At the high working temperature of > 300 °C, both the Na anode and the S cathode are liquids, dramatically increasing the operational cost and decreasing safety due to potential fires and explosions caused by the catastrophic failure of the thin ceramic SE⁷. In contrast, ambient-temperature ASSSBs using solid Na metal anodes are significantly more desirable, not only because of their lower cost, but also because of their lower temperature operation, T < 100 °C, which enables them to be more safely used in a broader range of applications. However, when operated such that the Na metal anode is now in solid state, not only must the SE be resistant to direct chemical and electrochemical reaction with Na, it must also be resistant to solid metallic sodium dendrite penetration. Therefore, the search for new SEs for ASSSBs must simultaneously meet the stringent requirements of low cost and facile fabrication, but also meet severe mechanical and chemical stability requirements. So far, no single sodium SE has been able to simultaneously meet all four of these requirements, and therefore, the development of SEs that are stable while cycling solid Na metal remains a great challenge.

Inorganic SEs can be divided into three categories: ceramic, glass-ceramic, and glass. Ceramic SEs such as β"-Al₂O₃ and NASICON-type oxides exhibit excellent chemical stability towards Na metal. Nevertheless, their high Na-ion conductivities are achieved only when they are processed to near theoretical densities, requiring sintering temperatures in excess of 1,500 °C for long hours, and are subjected to poor wettability with Na metal due to their rigid and rough

surface^{8,9}. Furthermore, it has been observed that Na metal preferentially propagates along distinct grain boundaries, forming dendrites that eventually short circuit the electrolyte^{10,11} (Fig. 1a). This has been a source of controversy in the field of SEs because these ceramic oxide SEs have mechanical moduli in excess of 200 GPa and provide more than adequate elastic and shear moduli to resist Na dendrite. Glass-ceramic SEs (e.g., heat-treated Na₃PS₄, simplified as HT–Na₃PS₄) and other sulfide SEs have compliantly soft surfaces that exhibit less well-defined grain boundaries due to the existence of a certain quantity of a glassy phase (5~50 vol%), which can mitigate the dendrite formation and growth. It turns out, however, that when these SEs come into contact with Na metal, they break down into an unstable solid electrolyte interphase (SEI) layer ¹²⁻¹⁵ (Fig. 1b). Because of these reasons, Na alloys like Na–Sn are often used as an anode. These alloys raise the voltage on the anode and decrease the energy density.

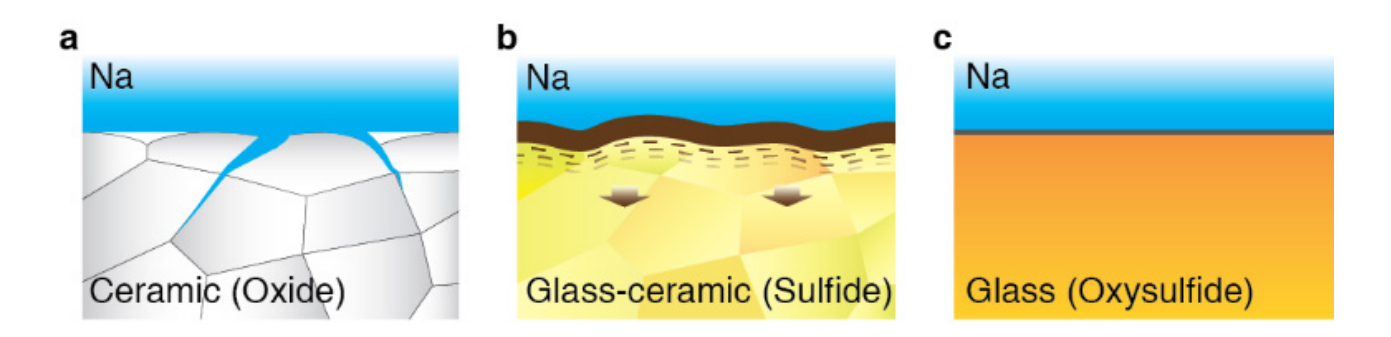


Figure 1. Three types of solid electrolyte-Na metal interfaces.

To date, there is no single SE that can simultaneously meet all of the mechanical, chemical, electrochemical, and processing requirements that can enable the ASSSBs with enhanced electrochemical performance and specific energy. We have recently reported the improved chemical stability of the mixed oxy-sulfide Na₃PS₃O SE in contact with metallic Na compared with pure sulfide SE¹⁶. Here, knowing the specific benefits of the individual SEs described above, and recognizing the inherent cost, process, and scale-up advantages of mechano-chemical milling

(MCM), we report in this work a series of Na₃PS_{4-x}O_x oxysulfide glass SEs that consist of a predominantly sulfide-based SE that is doped with small amount, up to 15 mol.% of oxygen (x = 0.60), that can be rendered fully chemically reacted from simple precursors by MCM and fully glassy and homogeneous by pressure sintering at room temperature.

These new glass SEs begin as fine-grained and agglomerated powders as a result of the MCM processing and feature properties and structures that are strongly dependent on the oxygen doping. We have observed that during normal uniaxial pressing at pressures less than 300 MPa, these SEs spontaneously transform into fully dense and microscopically and macroscopically homogeneous smooth glasses that behave as if they had been melt quenched (MQ) to the normal glassy state. Their homogeneous structures appear to be isostructural to glasses of the same composition produced by normal MQ processes. This structural transformation appears to be unique among oxysulfide SEs at the reported oxygen doping levels. We have found that the formation of the homogenous bulk glassy phase is an essential property of these SEs in order to be mechanical, chemical, and electrochemically stable against Na metals (Fig. 1c).

The ternary composition of Na₂S–P₂S₅–P₂O₅ reported here has been carefully designed according to five rules: first, P₂S₅ is a strong glass former that appears to facilitate the formation of a structurally homogeneous bulk glass, which we find is crucial to suppressing the Na dendrites propagation^{17,18}. Second, following previous studies of oxysulfide glasses where the added oxygen preferentially forms structure enhancing bridging oxygen (BO), the glass network can be reinforced with stronger chemical bonding of P–O compared to that of P–S¹⁹, thereby boosting the mechanical strength^{15,20,21}. Third, following our previous observations on binary Na₂S + P₂S₅ glasses^{22,23}, made either by MCM or MQ techniques, maximum Na-ion conductivity was observed at maximum Na₂S concentration. Fourth, pure sulfide glasses always exhibit superior Na-ion

conductivities over pure oxide glasses²⁴⁻²⁷. And fifth, again following our previous observations²⁸ and those of Hayashi et al.²⁹, that in mixed oxysulfide glasses, the conductivity rapidly increases with small sulfur replacements, < 25 mol.%, but then decreases after this maximum.

In this work, we conducted a systematic characterization of the sodium phosphorous oxysulfide SE, Na₃PS_{4-x}O_x (NPSO), where $0 \le x \le 0.60$, by examining their chemical structures, mechanical properties, the composition and thickness of SEI formed at the SE-Na interface, and their overall electrochemical performance as measured in Na|SE|Na symmetric cells. Their performance at both reducing and oxidizing potentials was examined by forming and successfully cycling ambient-temperature sodium-sulfur batteries. We believe these mixed oxysulfide SEs and their unique homogenous bulk glassy structure produced by room-temperature pressing provide a new paradigm in the development of safe, low-cost, energy-dense, and long-lifetime ASSSBs.

Results and Discussion

Formation of Chemically Reacted Glasses. The synergistic effects of oxygen additions on the properties of the NPSO SEs were examined for different compositions of x = 0, 0.15, 0.30, and 0.60 that were synthesized via the high-energy MCM and systematically characterized. The XRD patterns (Supplementary Fig. S1) show that all the raw materials became amorphous after MCM, as no diffraction peaks of the starting materials were detected. Hayashi et al. and we have observed that unreacted Na₂S and P₂S₅ were observed for MCM time shorter than those used here and that unreacted Na₂S was observed for Na₂S contents higher than those used here^{22,30}. Chemical spectroscopies, infrared (IR), Raman, nuclear magnetic resonance (NMR), and X-ray photoelectron spectroscopy (XPS) were used to demonstrate the full chemical reaction between Na₂S and P₂S₅, rather than just amorphization of the starting materials. The DSC curves in Supplementary Fig. S2 further reveal that all of the amorphous samples are glassy, exhibiting a

glass transition (T_g) around 200 °C. It needs to be pointed out that, for all of the glass samples, the glass formers are relatively poor and readily crystallize upon heating only slightly above the T_g of the glass. This rapid crystallization "cuts off" the full observation of the glass transition in these glasses and, as such, causes the T_g to be a very weak signature. The DSC trace of the x = 0.15 glass shows this effect of crystallization right after entering the glass transition. However, for the oxysulfide SEs ($x \ge 0.30$), the working range, or the difference between T_g and T_c , becomes larger with increasing oxygen content, indicating adding oxygen results in greater resistance to crystallization.

While a complete understanding of the complex mechano-chemical processes taking place during high-energy MCM is yet not fully known, it is generally agreed that MCM generates high local temperatures during the rapid ball-to-material-to-wall and ball-to-material-to-ball collisions and generates rapid thermal quenching after the collision as the materials are thermalized back to the near room temperature of the reaction vessel. The combination of high local temperature and rapid quenching is believed to be responsible for the formation of amorphous materials that also exhibit a liquid state glassy Tg. However, just as in MQ systems, the quenching rate is not always sufficient to yield a fully amorphous glass and the presence of small amounts of crystalline phases can be detected in some systems, which was recently observed in the Na₂S–P₂S₅ system³¹ and the Li₂S–P₂S₅ system³².

To examine in more detail the possible formation of small amounts of fine-grained crystalline phases in the NPSO SEs during the MCM process, high-energy synchrotron XRD patterns were collected and shown in Fig. 2a. All synthesized SEs feature two broad halos superimposed with weak Bragg peaks, indicating that a small number of fine-grained crystalline phases do form and are embedded in the majority of an otherwise glassy matrix. The SEM images

(Supplementary Fig. S3) of the x = 0.15 SE show that the major glassy powders are distributed in the range of 2 to 8 µm with an average particle diameter of 5.3 µm. The TEM image and FFT pattern (Supplementary Fig. S4) further reveal that the crystalline phase in the glassy matrix is tetragonal Na₃PS₄ (t-Na₃PS₄). However, as seen in Fig. 2a, when x reaches 0.60, these crystallization processes weaken, as evidenced by the fact that the t-Na₃PS₄ peak has almost disappeared. However, it is now replaced by the appearance of crystalline Na₂S that may arise from an incomplete chemical reaction.

The reason for the appearance of Na₂S at the higher O substitution was examined by Raman spectroscopy since it is sensitive to sulfur-containing units. According to Fig. 2b, the main feature peak²⁵ at 420 cm⁻¹ is the stretching mode of the PS₄ unit, which is a non-bridging sulfur (NBS) unit, identified as P⁰ unit^{24,30} where the superscript 0 is the number of bridging oxygens (BOs) on this short range order (SRO) unit. The Gaussian fitting of this mode (Supplementary Fig. S5) suggests that with the incorporation of oxygen, a small population of the original P⁰ units disproportionate into P¹ units (containing one bridging sulfur (BS), e.g. P₂S₇) with the liberation of sodium sulfide $(2P^0 \rightarrow 2P^1 + Na_2S)^{24}$ to balance charge. This disproportionation reaction is supported by the observation of Na₂S peaks in the synchrotron XRD results. The mode centered at 380 cm⁻¹ is assigned to the P₂S₆ unit, which possesses a homopolar P-P bond that decreases in concentration with the oxygen addition³³. The formation process of the P₂S₆ defect unit generates residual sulfur species (e.g. sulfur element) that show a characteristic Raman mode arising from the -S-S- linkage and occurs at 470 cm⁻¹. As indicated from both Fig. 2a and 2b, except for a small amount of crystalline phases of Na₃PS₄ and Na₂S, which we estimate to be in the range of < 5 mol.%, the main composition of the NPSO SEs is glass.

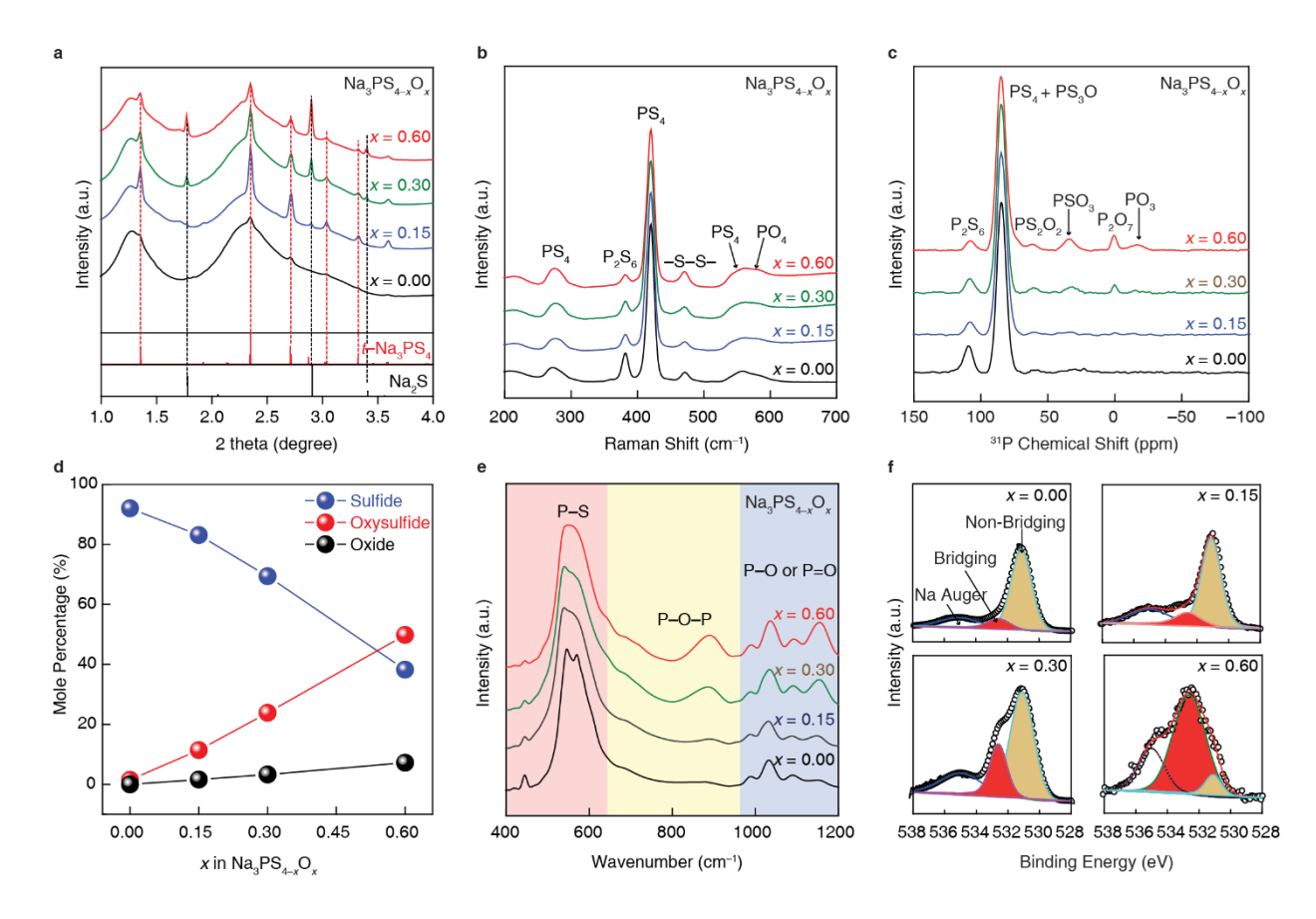


Figure 2. Structural characterizations of amorphous Na₃PS_{4-x}O_x (x = 0, 0.15, 0.30, and 0.60) SEs. Spectra from (a) Synchrotron X-ray diffraction, (b) Raman, (c) ³¹P NMR, (d) Structural units and their relative mole percentage, (e) Fourier transform-infrared spectra (FTIR), and (f) O 1s X-ray photoelectron (XPS).

Chemical Short-Range Order. ³¹P MAS–NMR was used to gain further insights into the glassy phase of these NPSO SEs by examining the local structure around the phosphorus glass-forming cation. The deconvolution of the ³¹P NMR spectra (Fig. 2c) shows that the glass Na₃PS₄ (x = 0) is composed mainly of PS₄ (82 ppm) and P₂S₆ (108 ppm) units, which is consistent with the Raman spectra described above. With the incorporation of oxygen, three new peaks attributed to the formation of mixed oxysulfide and oxide units, PS₂O₂ oxysulfide (63 ppm), PSO₃ oxysulfide (32 ppm), and P₂O₇ oxide (3 ppm), can be clearly observed³⁴. The peak for the PS₃O oxysulfide units

that were supposed to be there but aren't is almost impossible to see because it has almost the same chemical shift as the PS₄ units²⁹.

However, following the methods we proposed before 24,35 , this unit and its relative fraction of all of the SRO units were determined by careful spectral deconvolution and corrected for charge balance among the Na⁺ ions and the various PS_{4-x}O_x anions. The composition dependence of the population of the various SRO structural units in these oxysulfide NPSO SEs is given in Fig. 2d and shows that, as expected, the fractions of mixed oxysulfide units dramatically increase with oxygen doping level and become the dominant species when x reaches 0.60. The appearance of PS_{4-x}O_x oxysulfide SRO units suggests that oxygen has been incorporated into the P–S tetrahedral unit. Due to the much stronger chemical bonding of P–O compared to that of P–S¹⁹ and the bridging oxygens that can microstructurally connect the units to a more robust and homogeneous glass network, the mechanical strength of the SEs after oxygen incorporation were expected to be improved.

FTIR spectroscopy was further applied to explore the chemical bonding between phosphorus and sulfur and phosphorous and oxygen. The FTIR spectra shown in Fig. 2e can be divided into three parts corresponding to terminal P–S⁻ (400–600 cm⁻¹), BO P–O–P (600–950 cm⁻¹) and terminal non-bridging oxygens (NBOs) P–O⁻ or P=O (950–1200 cm⁻¹) modes, respectively^{36,37}. Detailed peak assignments are listed in Supplementary Table S1. It is evident that oxygen incorporation into the glass matrix leads to a slightly increased fraction of P–O⁻ and P=O bonds and a particularly significant increase in the fraction BO P–O–P bonds, where the O atom is bridging between two phosphorus atoms. Further evidence of the formation of BOs on adding oxygen to Na₃PS₄ can be found in O 1*s* XPS spectra (Fig. 2f), showing the BO with a binding energy of 532.5 eV^{38,39} accounts for the higher fraction of the oxygen for larger *x* values in NPSO

SEs. Spectral deconvolution of Na₃PS_{3,4}O_{0.6}, for example, shows that more than 90% of the added oxygen atoms are present as BOs in the glass. This behavior is completely consistent with our previous work⁴⁰ where in a similar Li₂GeS_{4-x}O_x glass, the added oxygen was also found to preferentially replace S in the bridging sulfur (BS) positions until all of the BSs were eliminated. The oxygen did not form NBOs until there were no more BSs to replace. The results here for the NPSO series reveal a more complex mechanism for the added oxygen to form BO because in the present system, there are no BSs to begin with. Hence, the added O forces the formation of the disproportionation reactions described above. To maintain charge balance in the series, the formation of a BO requires the formation of "free" Na₂S in direct proportion to the amount of oxygen added. While overall charge balance appears to be maintained in this system, the formation of BOs through the addition of oxygen also forms increasing chain units in the form of P¹ units. We have observed this same behavior in the slightly lower modifier Na₄P₂S_{7-x}O_x system³⁵.

Homogeneous Glass with Improved Mechanical Properties. A homogeneous and mechanically robust SE is a prerequisite for successfully cycling with Na metal anodes¹¹. Consequently, the morphological structure and the mechanical properties of NPSO SEs were investigated. For comparison, the widely studied heat-treated Na₃PS₄ glass-ceramic SE (HT–Na₃PS₄) was also studied^{25,41}. Pores and grain boundaries are clearly observed in the SEM images of pelletized HT–Na₃PS₄ (Fig. 3a–b). These surface defects are believed to induce dendrite formation, subsequent dendrite propagation^{42,44}, and eventual short-circuit through the SE, as demonstrated in Supplementary Fig. S6. Na₃PS₄ glass SE, however, shows fewer structural pores compared to HT–Na₃PS₄. In sharp contrast to both of these SEs, the surface of the NPSO glass SE appears to be free of pores from the surface through to the interior.

To the best of our knowledge, this fully homogeneous and dense glassy morphology induced by simple, low-cost room temperature uniaxial pressing is observed here for the first time in any SE fabricated by simple cold-pressing. Such a morphology is presumably closely related to the outstanding formability of NPSO. As shown in Fig. 3a–b and Fig. S7, this phase is nearly fully densified at a pressure as low as 150 MPa. In comparison, Na₃PS₄ glass and HT–Na₃PS₄ couldn't achieve a similar relative density even when much higher pressures were applied, as seen from Fig. 3c. The excellent formability of these oxysulfide SEs is attributed to the synergistic effects of mixed P₂S₅ and P₂O₅ glass formers, which not only build a close-packed glass network with abundant BO units but also facilitate the local sintering process of the powders as demonstrated by more interparticle adhesion and necking compared to the pure sulfide SEs particles (Supplementary Fig. S8). Overall, for oxysulfide SEs, their unique formability and homogeneous structure will undoubtedly enhance their mechanical strengths and reduce the likelihood of dendrite-induced short-circuit when using the Na metal anode, as described in Fig. 1a.

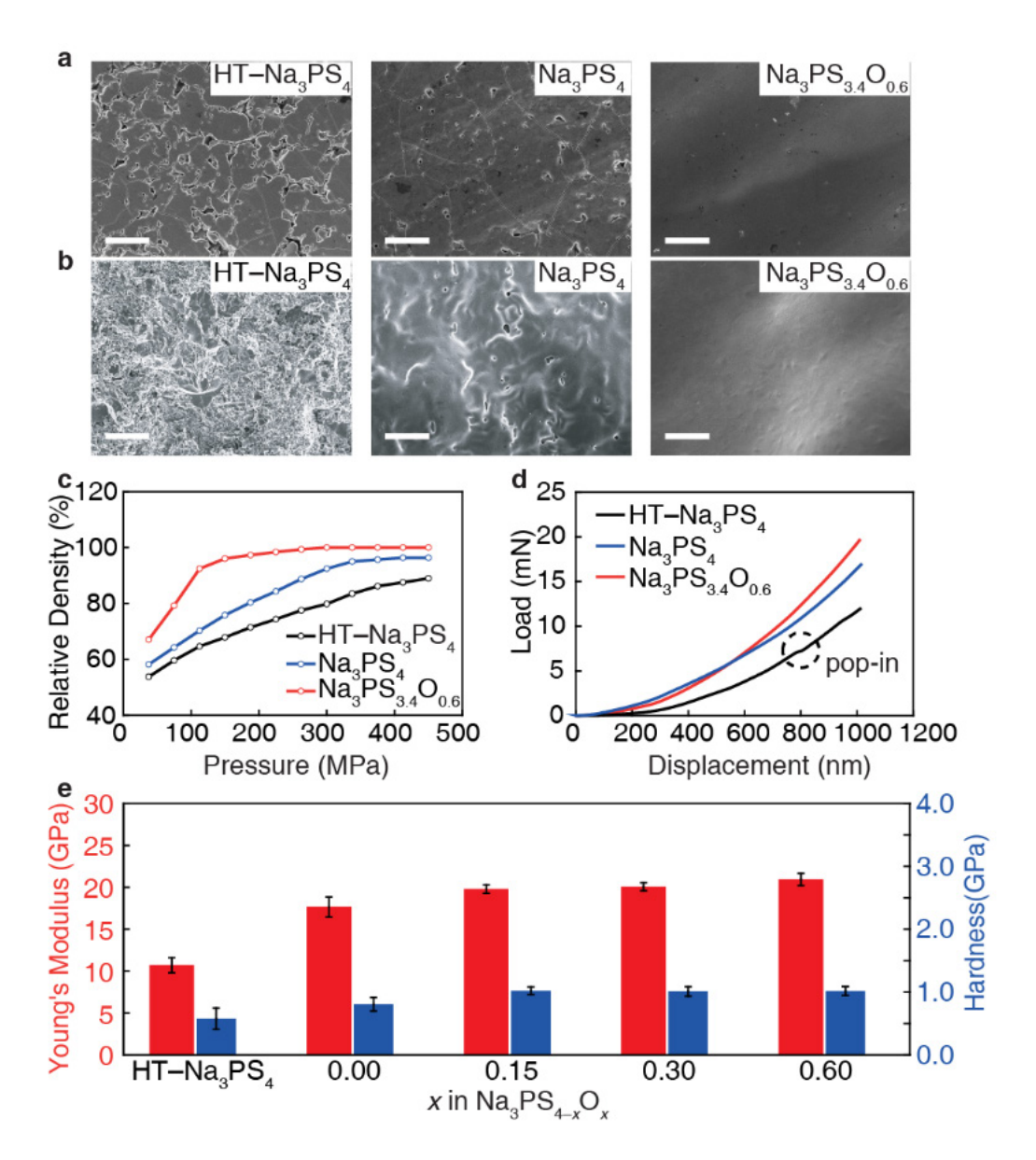


Figure 3. Mechanical properties of Na₃PS_{4-x}O_x glass SEs (x = 0 and 0.60) and HT-Na₃PS₄ glass-ceramic SE. (a) Surface and (b) cross-sectional morphology, scale bar 10 μ m; (c) Relative density vs. fabrication pressure; (d) Nanoindentation loading curves; error bars indicate the standard deviation of nine tests; and (e) Young's modulus and hardness of various SEs. HT-Na₃PS₄ represents the heat-treated Na₃PS₄ glass-ceramic electrolyte.

To quantify the mechanical properties of SEs, two critical parameters: Young's modulus E and hardness H were measured using the nanoindentation technique⁴⁵. Typical load-displacement curves in Fig. 3d and Supplementary Fig. S9 show that the HT-Na₃PS₄ pellet experiences a sudden increase in indenter penetration during the loading process, which is not found in glassy NPSO SEs. This is referred to as "pop-in" and is associated with the generation of a crack^{45,46}. This behavior indicates that the HT-Na₃PS₄ SE is more brittle than its glassy counterparts. Such a cracking is certainly unfavorable for the preparation and practical application of SEs. Further, benefiting from the homogeneous property of the glassy materials, the NPSO SEs display very small standard deviations for E and H as seen in the bar chart in Fig. 3e. Moreover, oxygen doping results in an increase of E and H of SEs, which supports the observation that oxygen doping produces more BO units in the glass network, thus providing more homogeneous and robust mechanical properties. The E and H of Na₃PS_{3.4}O_{0.6} glass were measured to be 20.9 ± 0.7 GPa and 1.0±0.1 GPa, respectively, which is the highest among the NPSO series and even higher than those of the reported sulfide-based Li-ion and Na-ion SEs prepared by hot-pressing 18,47,48. Assuming that Poisson's ratio v is ca. 0.3 according to the study by Sakuda et al.⁴⁹, the shear modulus G of Na₃PS_{3.4}O_{0.6} glass is ca. 8.0±0.3 GPa, which is believed to be sufficient to suppress dendritic penetration of Na metal as predicted by the Monroe and Newman criterion⁵⁰.

Characterization of the Na–SE interface. We first examined the Na–NPSO interface using time-dependent electrochemical impedance spectroscopy (EIS) and XPS. Na|NPSO|Na symmetric cells were fabricated to monitor the evolution of the EIS spectra and the area specific resistance (ASR) over a period of 5 hours of resting and this is shown in Fig. 4a and Supplementary Fig. S10, respectively. The obtained EIS spectra can be divided into three semicircle regions,⁵¹ and the fitting parameters are listed in Supplementary Table S2. The high-frequency semicircle represents

the combined bulk and grain boundary resistance and capacitance $(R_b + R_{gb}, C_b + R_{gb})$ of the SEs; the mid-frequency semicircle with the characteristic capacitance of $10^{-6} \sim 10^{-7}$ F arises from the interfacial resistance and capacitance (R_i, C_i) of SEI formed between Na and SE⁵². As seen from Table S2, the added oxygen has a positive effect on improving the observed stability against Na metal. Fig. S10 shows that the change of ASR becomes less significant when more oxygen is doped.

To identify the composition of SEI that apparently grows with time for the $x \neq 0.60$ glassy NPSO SEs, Na metal was detached from the symmetric cells and the surface of SEs was probed by the XPS. Compared to the surfaces of the pristine SEs (Supplementary Fig. S11), Fig. 4b–4c shows that the surfaces of the Na₃PS_{4-x}O_x, x = 0, 0.15, and 0.30, SEs exhibit two new pairs of doublets for P 2p spectra and S 2p spectra at lower bonding energy after contacting with Na metal. These new pairs of doublets correspond to the reduced phosphide and sulfide species, respectively. According to the theoretical calculation from Tian et al.¹² and the experimental study from Wenzel et al.¹³, these reduced species are Na₂S and Na₃P, respectively, the latter of which is a mixed ionic and electronic conductor that can cause continuous reduction of the SE. Similar effects have been found in other pure sulfides and selenides, such as Na₃PS₄, Na₃SbS₄, Na₃PSe₄, and while they all have high ionic conductivities, their tendency to produce these unstable SEIs renders them unsuitable for use in Na-metal batteries¹⁴. In contrast, Fig. 4b–c shows that these same XPS signals from these reduced species are nearly indistinguishable above the baseline noise in the S 2p and P 2p spectra for the Na₃PS₃,4O_{0.6} SE.

We used the Time-of-Flight Secondary Ion Mass Spectrometry (ToF-SIMS) to better understand the composition of the SEI layer at the Na|SE interface. The selected mass spectra of the surfaces of the two solid electrolytes (Na₃PS₄ and Na₃PS_{3,4}O_{0.6}) after Na metal removal are

shown in Supplementary Fig. S12. Two strong peaks at 55.0 m/z and 192.8 m/z correspond to NaS⁻ and Na₃P₄⁻ fragments, respectively, in the Na|Na₃PS₄ sample (black). The depth profile of these two fragments during Cs⁺ ion sputtering is shown in Fig.4d. It is reasonable to assign the two fragments to Na₂S and Na₃P as a result of Na₃PS₄ reduction: $8Na + Na_3PS_4 \rightarrow 4Na_2S + Na_3P$. We estimate the thickness of the SEI based on the profile of Na₃P₄ fragment because Na₃P is electronically conductive, which dictates the extent of electrolyte decomposition. The thickness of the SEI in the Na|Na₃PS₄ sample corresponds ~1000 seconds of Cs⁺ sputtering. In contrast, the intensity of Na₃P₄⁻ at surface (~10⁻⁵ in the Na|Na₃PS_{3,4}O_{0,6} sample) is three orders of magnitude lower than in the Na|Na₃PS₄ sample (~10⁻²). Furthermore, the intensity drops to 10⁻⁶ after only 100 seconds of sputtering. This comparison shows, in the case of the Na|Na₃PS_{3.4}O_{0.6} sample, the initial reduction of SE is suppressed by a factor of 1000 and the thickness of SEI layer is reduced at least by a factor of ten. After initial SEI formation, the interface stabilizes and Na metal plating process initiates. We hypothesize that the self-passivating nature of Na₃PS_{3.4}O_{0.6} decomposition products is owing to the formation of electrically insulating Na₂O, the signal of which is too weak to detect in the ToF-SIMS spectra due to the negligible SE reduction. Other fragments in Fig. 4e, including $P_2O_7^-$ (174.0 m/z), $Na_2PO_4^-$ (140.9 m/z), and $Na_2PS_4^-$ (204.8 m/z), are all derived from the bulk of Na₃PS_{3.4}O_{0.6}, which exhibits flat profiles during Cs⁺ sputtering. To our knowledge, this is the first sulfide-based fully homogeneous glassy SE that produces a self-passivating, thin SEI against Na metal.

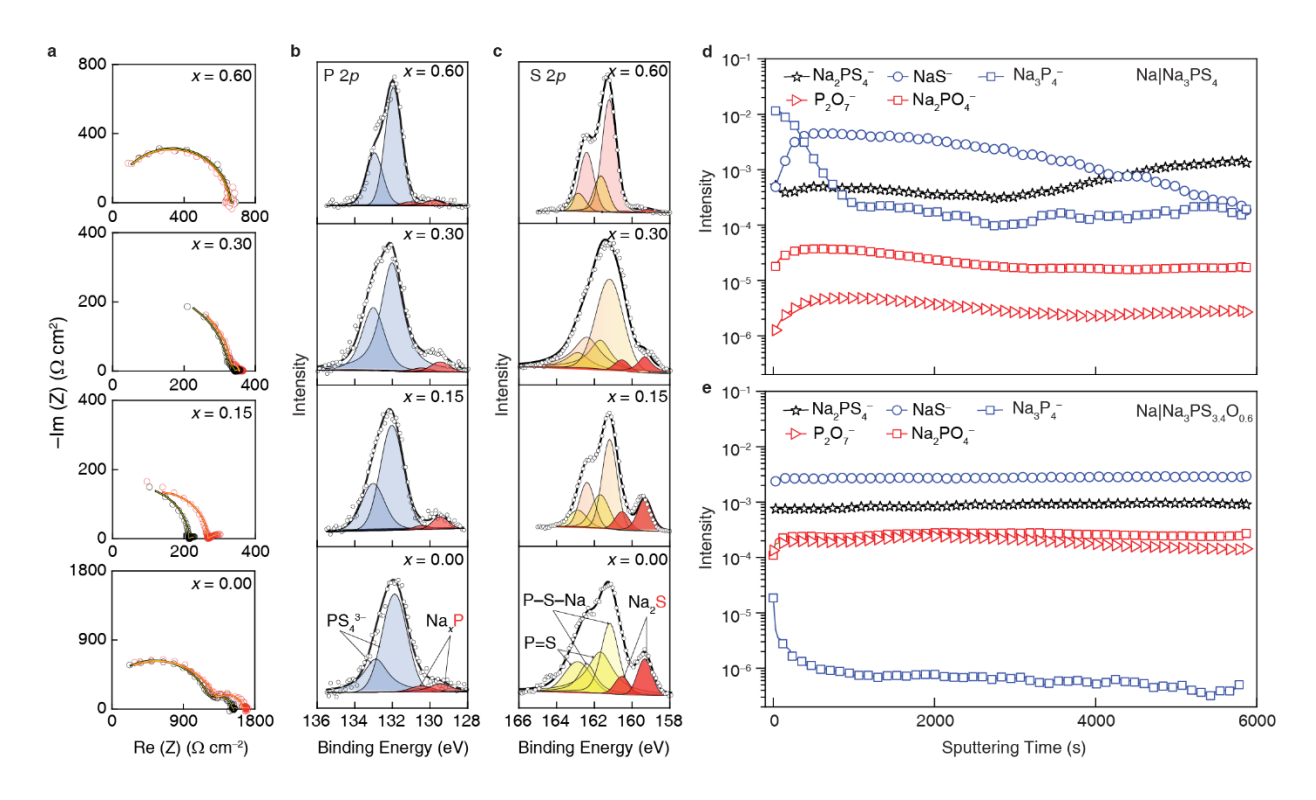


Figure 4. Chemical stability of Na₃PS_{4-x}O_x (x = 0, 0.15, 0.30, and 0.60) SEs towards Na metal at 60 °C. (a) Electrochemical impedance spectra (EIS) evolution of freshly made Na|SE|Na symmetric cells (black curve) vs after 5 hours of rest (red curve); XPS spectra of (b) P 2p and (c) S 2p for the interface between Na and SE; (d–e) Depth profiles of fragments from the ToF-SIMS spectra of the Na|Na₃PS₄ and Na|Na₃PS_{3.4}O_{0.6} interfaces after 5 hours of contact.

Electrochemically Stable Tri-Layer Composite SEs. Fig. 5a shows the temperature-dependence of the Na⁺ ionic conductivities that were obtained from the Nyquist plots (Supplementary Fig. S13) for the Na₃PS_{4-x}O_x, x = 0, 0.15, 0.30, 0.60. From Supplementary Fig. S14, it is intriguing that the ionic conductivities exhibit a 6-fold increase with the initial addition of oxygen, x = 0.15, rendering the conductivity of the Na₃PS_{3.85}O_{0.15} SE as high as 2.7×10^{-4} S cm⁻¹ and activation energy as low as 41.5 kJ mol⁻¹. This unusual rise in ionic conductivity could be attributed to two unique effects

of the addition of oxygen to the base Na₃PS₄ glassy SE. First, in a recent study²⁸, we found that doping oxygen into the comparable Li₂GeS_{2-x}O_x glassy SE enhanced the free volume available to the mobile Li⁺ ion for conduction. As a result, the 'doorway' radius, r_D , between Li⁺ ion sites increased, lowering the overall activation energy and increasing the conductivity²⁸. The compositional similarity and the similar sharp increase in the conductivity suggest a similar underlying mechanism for Na₃PS_{4-x}O_x and Li₂GeS_{2-x}O_x glassy SEs. Second, as shown by the synchrotron XRD data in Fig. 2a, the presence of a highly conductive t-Na₃PS₄ crystalline phase²⁵ may introduce a second highly conductive parallel phase in the glass matrix, albeit in a less than 5 mol.% fraction, resulting in enhanced overall conductivity⁵³.

Additions of oxygen monotonically increase the activation energy thereby decreasing the conductivity. Consistent with our previous studies²⁸, the added oxygen shrinks the structure, reducing the free volume available for conduction and boosting activation energy through the formation of more BO units. Further decreasing the conductivity is the formation of a very poorly conductive Na₂S phase formed through the disproportionation reaction described above. As a result, at 60 °C, the Na₃PS_{3,4}O_{0.6} SE has a reduced conductivity of 8.2×10⁻⁵ S cm⁻¹. Furthermore, it has been recently reported that high electronic conductivity of SEs, as well as internal defects (cracks, pores, grain boundaries) are responsible for the creation and propagation of Li dendrites in SEs^{54,55}. Fig. 5b compares the electrical conductivity of Na₃PS_{3,4}O_{0.6}, Na₃PS₄, and HT–Na₃PS₄ using ion-blocking electrodes. The electrical conductivity of Na₃PS_{3,4}O_{0.6} is two orders of magnitude lower than that of HT–Na₃PS₄, suggesting the unique homogeneous microstructure of oxysulfide SE, which will surely reduce the chance of dendrite-induced short-circuit.

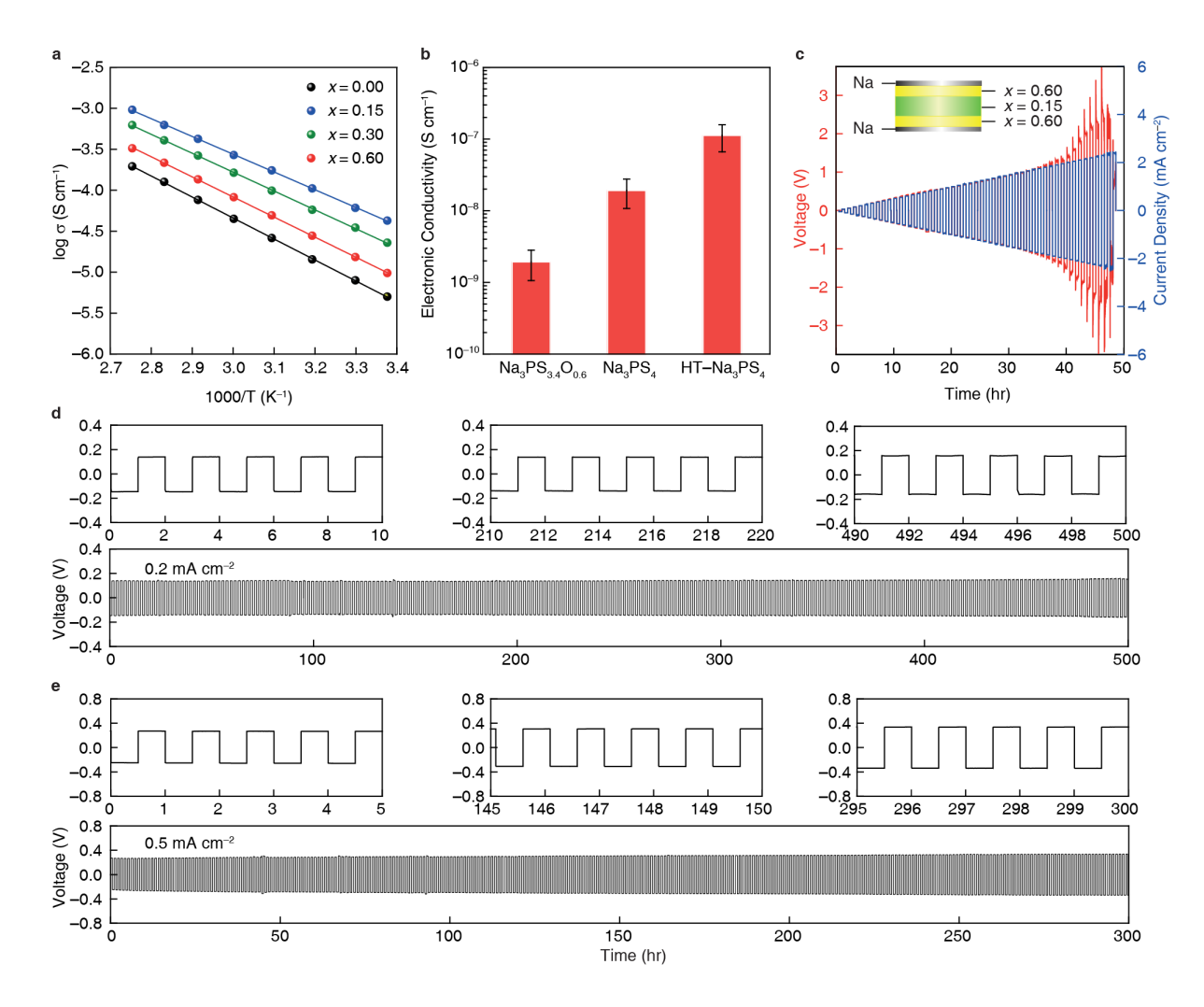


Figure 5. Electrochemical properties of glassy oxysulfide SEs. (a) Temperature dependence of the Na-ion conductivities of SEs; (b) Electronic conductivity of three types of SEs measured by two-blocking electrodes at 60 °C, error bars indicate the standard deviation of three tests; (c) Critical current density (CCD) test of a tri-layer SE in Na|SE|Na symmetric cell (SE is Na₃PS_{3.4}O_{0.6}|Na₃PS_{3.85}O_{0.15}|Na₃PS_{3.4}O_{0.6}) at 60 °C. The step current density increase is 0.05 mA cm⁻² and plating/stripping period is 0.5 hour each; (d, e) Galvanostatic cycling of the symmetric cells at 60 °C with current densities of 0.2 mA cm⁻² and 0.5 mA cm⁻², respectively. HT–Na₃PS₄ represents the heat-treated Na₃PS₄ glass-ceramic electrolyte.

However, the excellent formability of the Na₃PS_{3.4}O_{0.6} SE allows for the fabrication of a thin SE layer with very low resistance. A perfect SE for ASSSBs requires both high ionic conductivity as well as excellent mechanical and chemical stability. To produce such an SE, a trilayer architecture was designe with the most ionically conductive Na₃PS_{3.85}O_{0.15} in the inside and the mechanically and chemically stable Na₃PS_{3.4}O_{0.6} on the outside, as in the inset of Fig. 5c. Supplementary Fig. S15 shows a fully all-glass SE separator without any discernible voids or grain boundaries was attained owing to the excellent formability and densification. The cyclability of the tri-layer electrolyte was investigated in a symmetric Na|SE|Na cell using gradient-current and constant-current experiments, as illustrated in Fig. 5c-e. The voltage profile of the tri-layer separator shows an ohmic response, V = IR; however, sudden voltage spikes occur when the current exceeds 2.3 mA cm⁻², which was estimated to be the critical current density (CCD) for the tri-layer SE. The highest recorded CCD value for sulfide-based Na-ion SEs is 2.3 mA cm⁻², which is also equivalent to the state-of-the-art CCD value of lithium-based sulfide SEs. The improved capability to resist Na dendrite formation and penetration is ascribed to their homogeneous and porosity-free structure, as well as their robust mechanical properties. These findings are consistent with Porz et al.'s11 conclusions on the failure processes of SEs toward a metal anode, in which they discovered that Griffith's flaws in the SEs cause dendritic growth and propagation across SEs.

At current densities of 0.2 mA cm⁻² and 0.5 mA cm⁻², symmetric cells with tri-layer electrolytes can cycle for hundreds of hours without short-circuiting, as shown in Figs. 5d–e. The inserts to Figs. 5d–e show that remarkably flat voltage profiles are recorded at each cycle over the duration of the cell's cycling. This behavior suggests that the Na plating and stripping processes are quite stable at the Na₃PS_{3.4}O_{0.6}|Na interface, which is consistent with the previous explanation. The charge-transfer resistance for Na₃PS_{3.4}O_{0.6}|Na is only 10 Ω·cm². Supplementary Fig. S16

compares this study to some state-of-the-art findings on Na|SE|Na symmetric cells for various kinds of known Na-ion conducting SEs. This figure depicts three key parameters that influence the energy density, power density, and cycle life of full cells: the capacity of Na metal plated per cycle (area of the circle), current density, and cycling time. It is clear that the composite tri-layer oxysulfide SE produced in this work greatly improves the cycle duration and current density performance of SEs cycling Na in symmetric cells. It is worth noting that the mass transport in Na metal is sufficient to support stable cycling without the introduction of interfacial voids⁵⁶. In particular, our composite tri-layer SE sets new standards for higher current density and longer cycling duration in ASSSBs.

As previously demonstrated, the Na₃PS_{3.4}O_{0.6} SE can be coupled with Na₃PS_{3.85}O_{0.15} to form a stable all-glass separator. Similarly, by employing a tri-layer design, Na₃PS_{3.4}O_{0.6} can be used for couple with glass-ceramic SEs, e.g. HT–Na₃PS₄, or Na₃SbS₄. Supplementary Fig. S17 shows an example of this for Na₃PS_{3.4}O_{0.6}|HT–Na₃PS₄|Na₃PS_{3.4}O_{0.6}. Excellent interfacial contact may be formed between these two SEs due to the ease with which the Na₃PS_{3.4}O_{0.6} SE deforms under pressure to form a homogeneous interface. Because HT–Na₃PS₄ SE has a comparable conductivity (3.9×10⁻⁴ S cm⁻¹)⁵⁷ to Na₃PS_{3.85}O_{0.15} SE, Fig. S17 demonstrates that the Na|tri-layer SE|Na symmetric cells have a very similar overpotential to the symmetric cells illustrated in Fig. 5d–e. Furthermore, stable Na plating/stripping profiles at 0.2 mA cm⁻² were achieved for up to 500 h and up to 240 h at 0.5 mA cm⁻².

All-solid-state Na–S Full Cells. The excellent Na₃PS_{3,4}O_{0.6}|Na stability enables the fabrication of ASSSBs, of which the ambient-temperature Na–S battery is one of the most promising because of its very low cost and high theoretical specific energy. On the basis of the above study that demonstrated the stability of the tri-layer SE in a Na metal symmetric cell, a Na–S battery having

the architecture of S-Ketjen Black (KB)-Na₃PS_{3.85}O_{0.15}|Na₃PS_{3.85}O_{0.15}|Na₃PS_{3.4}O_{0.6}|Na was designed and tested.

The voltage profiles for the cell operating within the voltage window of 1.0 to 3.0 V are shown in Fig. 6a. The cell has a high initial discharge capacity of 1280 mAh g⁻¹, which is 76% of the theoretical capacity of sulfur (Na \rightarrow Na₂S: 1675 mAh g⁻¹) and substantially higher than that the high-temperature Na–S battery⁵⁸, which has a capacity of 558 mAh g⁻¹. This is due to the fact that the Na-S battery presented here is an all-solid-state system without the discharge limit of Na →Na₂S₄ that the high-temperature Na–S battery has. The first cycle coulombic efficiency is 92%, indicating that the polysulfide shuttle phenomenon, which is frequent in liquid electrolyte-based cells, is not observed. After the first five cycles, the cell achieves ~100% coulombic efficiency. After 40 cycles, the reversible capacity stabilizes at around 1000 mAh g⁻¹ with a capacity retention of more than 80% (Fig. 6b). These values are much higher than those reported for Na-S batteries using oxide or polymer SEs and Supplementary Table S3 compares these previously reported solid-state Na-S batteries⁵⁹⁻⁶⁶ operating near ambient temperature to those described here. The discharge voltage profile consits two plateaus at 1.9 V and 1.25 V vs. Na/Na⁺, with a single slope in between. The average discharging potential is 1.42 V, which is higher than the discharging potentials of existing pure sulfide SE-based Na–S batteries with Na₁₅Sn₄ or Na₃Sb alloy anodes.

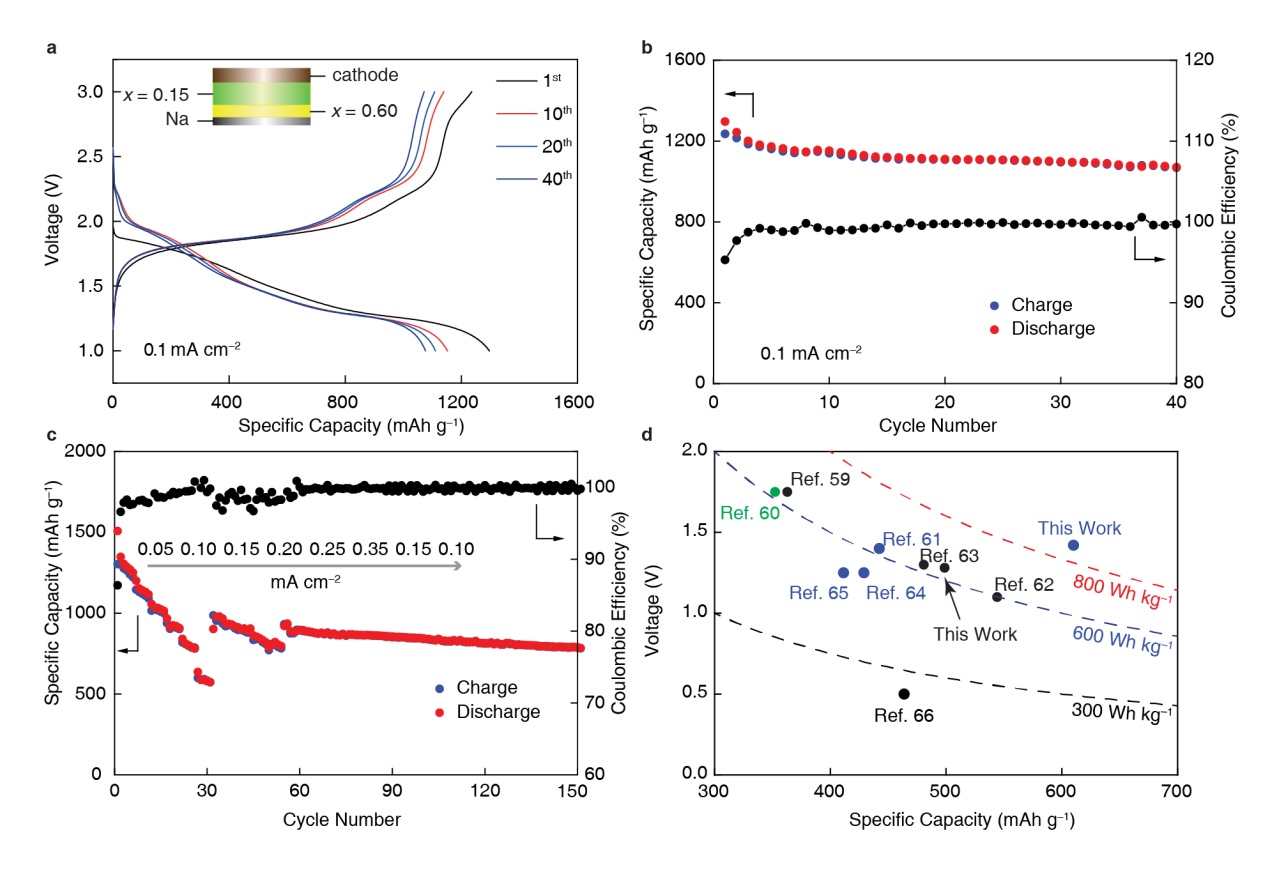


Figure 6. All-solid-state Na–S full cells measured at 60 °C. (a) Charge-discharge voltage profiles and (b) Capacity and coulombic efficiency vs. cycle number at a current density of 0.1 mA cm⁻²; (c) Rate capabilities of the Na–S full cell at various current densities (0.05–0.35 mA cm⁻²); (d) Summary of cell voltage–full cell capacity plot and material-level specific energy for reported ambient-temperature solid-state Na–S batteries (Room temperature: black; 60 °C: blue; 90 °C: green). Fig. S18 depicts the performance of a Na–S battery based on the oxysulfide SEs at ambient temperature. See Supplementary Table S3 for details. It is worth noting that the specific capacity in Fig. 6d depicts full-cell capacity while accounting for both the cathode and the anode.

The rate capability of our Na–S full cells was examined by cycling at increasing current densities. The cell can offer specific capacities of 1116, 908, and 574 mAh g⁻¹ at current densities

of 0.10, 0.20, and 0.35 mA cm⁻², as seen in the Supplementary Fig. S19. After the current was reduced to 0.10 mA cm⁻², the cell capacity restored to near-original levels, and and the cell cycled stably for 150 cycles (Fig. 6c). The significantly improved Na–S battery cycling performance is attributed to the excellent interface stability, which allows Na metal to plate/strip at high rates, the superior formability property of oxysulfide SEs, which ensures the consistently good contact with sulfur and carbon during cycling, and the overall solid nature of the SEs, which prevents any polysulfide shuttle between the anode and the cathode. As a result, among all currently reported all-solid-state Na–S batteries, the oxysulfide-based Na–S battery described here has the highest specific energy (Fig. 6d). For these reasons, we believe that these oxysulfide composite SEs could represent a completely novel and successful approach to the creation of low-cost, high-energy-density, safe, and long-cycle-life solid-state Na metal batteries.

In summary, a new class of oxysulfide glass SEs with the advantages of both sulfide and oxide SEs was successfully synthesized and systematically examined in both symmetric and full cell configurations. Oxygen-doped sulfide SEs have much stronger and denser glass networks than pure sulfide SEs due to the formation of greater concentrations of oxide and oxysulfide units with BO characteristics. Furthermore, while adding oxygen boosts the mechanical strength of the glassy SE, it also leads these oxysulfide SEs to demonstrate pressure-induced homogeneity of the glassy powder starting materials into homogeneous glass microstructure at ambient temperature. As a result of the greatly increased formability, the oxysulfide SEs exhibit higher mechanical strength and reduced electronic conductivity. Cells exhibit excellent electrochemical stability with Na metal through kinetic stability via the formation of a self-passivating SEI. A homogeneous trilayer composite SE including Na₃PS_{3,4}O_{0,6}|Na₃PS_{3,85}O_{0,15}|Na₃PS_{3,4}O_{0,6} can achieve a critical current density of up to 2.3 mA cm⁻², the highest recorded CCD value for Na-ion sulfide SEs, and

cycle stably at 0.2 mA cm⁻² for up to 500 h. Na–S full cells were fabricated using a composite oxysulfide bi-layer SE and were demonstrated to have the highest specific energy among solid-state Na–S systems to date. These new oxysulfide SEs, as well as the tri-layer composite SEs that they enable, could pave the way for the development of new glass electrolytes for high-energy, safe, low-cost, and long-cycle-life solid-state batteries in general, and all-solid-state Na–S batteries for energy storage devices in particular.

Methods

Synthesis of NPSO SEs. Na₂S, P₂S₅, and P₂O₅ (Sigma-Aldrich, 99%) were used as the raw materials without further purification. The Na₃PS_{4-x}O_x (x = 0.15, 0.30 and 0.60) SEs were prepared by high-energy planetary ball milling (MTI, MSK-SFM-1). Typically, 2 g mixtures of appropriate amounts of Na₂S, P₂S₅ and P₂O₅ powders were milled in an Argon-protected stainless steel jar containing stainless steel milling balls at 500 rpm for 3 h to obtain the amorphous SEs. Note different milling media and milling time were used in this work compared to Lazar et al. ¹⁶, which used ZrO₂-based milling media and 20 h of milling. Ball-milling raw materials in the agate jar at 500 rpm for 20 hours yielded pure sulfide x = 0 SE. By heating the glassy Na₃PS₄ under vacuum for 2 hours at 260 °C, the Na₃PS₄ glass-ceramic SE, abbreviated as HT–Na₃PS₄, was obtained. **Materials characterizations of NPSO SEs.** Because oxysulfide SEs are sensitive to air and moisture, all of the characterizations were carried out with Argon protection. To determine the crystallinity and the identity of the crystalline phases in the various SEs, lab-based X-ray diffraction (XRD) and synchrotron XRD patterns were collected using a Rigaku MiniFlex 600

with Cu K α radiation (λ = 1.5418 Å) and Beamline 11–ID–C at Advanced Photon Source with X-ray wavelength of 0.1173 Å, respectively.

The thermal behavior of the SEs powders was examined using differential scanning calorimetry (DSC) on a TA Instruments Q2000. The sample was placed in the Tzero aluminum pan and hermetically crimp-sealed inside the Argon-filled glove box. The DSC measurements were carried out at a heating rate of 20 °C min⁻¹ from 50 °C to 400 °C. A Renishaw inVia Raman spectrometer employing a 488 nm Ar⁺ laser and 10 mW of power was used to collect the Raman spectra from 200 to 700 cm⁻¹. SE powders were placed into a small plastic sample holder inside the glove box and covered with transparent tape to prevent exposure to air during data collection. Infrared (IR) spectra were acquired on a Bruker IFS 66 v/s vacuum IR spectrometer in the range of 400–1200 cm⁻¹ using a KBr beamsplitter. During the test, the spectrometer optical bench was held under vacuum to protect the samples from moisture and air. The samples' IR spectra were obtained by diluting the finely ground glass and glass-ceramic powders to 2% in finely ground and carefully dried CsI and then pressing them into tiny pellets. ³¹P Solid-state Magic Angle Spinning Nuclear Magnetic Resonance (MAS-NMR) spectra were collected using a JEOL ECA-500 NMR spectrometer. SE powders were packed into an alumina spinner with a sealant in an Argon-filled glove box. Spectra were collected using a 4.25 µs, 60° pulse length, and a 200 s recycle delay while rotating at 20 kHz. Chemical shifts were externally referenced to NaH₂PO₄.

The elastic modulus E and hardness H were determined using the same method as previously described⁴⁵. Briefly, E and H values were measured using a G200 Keysight nanoindenter equipped with a Berkovich tip. All the measurements were conducted inside an argon-filled glove box to eliminate moisture and air contaminations. To assure the convergence of the measured results, indentations with a maximum indentation depth of 1 μ m were pressed on

different spots of the SE surfaces. During the testing, the load-displacement curves up to pellet cracking were recorded and utilized to calculate the E and H using the Oliver-Pharr method. $H=\frac{P_{max}}{A}$, where P_{max} is directly determined from the prescribed load (i.e., 1 mN) and the contact area A is calibrated as a function of the contact depth. Reduced elastic moduli E_r is derived from the load-displacement response by $E_r = \frac{S\sqrt{\pi}}{2\sqrt{A}}$, where S is the slope of the unloading curve. Elastic modulus E is calculated from the E_r by taking into account the deformation of both the indenter and sample $\frac{1}{E_r} = \frac{1-v^2}{E} + \frac{(1-v_i^2)}{E_i}$ where modulus and Poisson's ratio of the diamond indenter (E_i , v_i) are 1141 GPa and 0.07, respectively; and the Poisson's ratio v is assumed to be 0.3.

Morphologies of the SEs powders, as well as the surface and cross-section of the densified pellets, were observed using a Gemini LEO 1525 scanning electron microscope (SEM). Nanocrystals embedded in the glass SE were confirmed using a JEOL 2100F transmission electron microscope (TEM). The X-ray photoelectron spectroscopy (XPS) spectra were collected using a Physical Electronics PHI 5700 on the SEs pellets using a monochromatic Mg K α X-ray source. The XPS signals were corrected relative to the C 1s signal (284.8 eV) and fitted using the XPSPEAK41 software. The relative density of the SEs was defined as $\rho_{\text{bulk}}/\rho_{\text{true}}$, where ρ_{bulk} is the bulk density and ρ_{true} is the true density of powders according to Nose et al.'s report¹⁸. ρ_{true} for Na₃PS₄ and Na₃PS_{3.4}O_{0.6} were 2.00 g cm⁻³ ¹⁸ and 2.28 g cm⁻³, respectively.

Time-of-flight secondary mass spectrometry (TOF-SIMS) was performed using a TOF-SIMS NCS instrument, which combines a TOF.SIMS 5 instrument (ION-TOF GmbH, Münster, Germany) and an in-situ Scanning Probe Microscope (NanoScan, Switzerland). A charge compensation with an electron flood gun was applied during the analysis. An adjustment of the charge effects was operated using suitable surface potential and extraction bias for the negative

polarity. The cycle time was fixed to 90 μ s (corresponding to m/z = 0–737 a.m.u mass range). All samples were transferred under an argon atmosphere with a transfer vessel (IONTOF GmbH) from the glovebox into the analysis chamber. High mass resolution spectra were performed in negative polarity to identify the chemical environment. A bunched 30 keV Bi³⁺ ions (with a measured current of 0.2 pA) was used as primary probe (scanned area 90 × 90 μ m²) with a raster of 128 × 128 pixels for analysis. The primary ion dose density was limited to 1.00×10^{12} ions per cm² for preserving the chemical composition and to achieve comparable measuring conditions between the measurements. A sputter ion beam (Cs⁺ ions at 2 keV energy with a current around 110 nA) with a raster of $300 \times 300 \ \mu$ m² was used for high mass resolution depth profile of ToF-SIMS in the negative polarization mode. The analysis area was placed in the center sputter crater to ensure a good quality of the depth profile. The beams were operated in non-interlaced mode, alternating 2 analysis cycles and 20 sputtering cycles followed by a pause of 5 s for charge compensation with an electron flood gun for controlling the sputter/ analysis rate ratio. All data evaluation was carried out with the software SurfaceLab 7.0 (IONTOF GmbH).

Electrochemical characterizations of SEs. The temperature-dependent ionic conductivities of the pelletized SEs were measured from 25 °C to 90 °C using alternating current impedance method (frequency: 1 MHz–0.1 Hz, amplitude: 5 mV) on a VMP3, Bio-Logic Co. electrochemical workstation. Before the measurement, the SEs powders were cold-pressed in a polyetherether-ketone (PEEK) test cell die (φ = 13 mm) under a pressure of 450 MPa and then co-pressed with 20 mg nano-copper powders (Sigma-Aldrich, 40–60 nm, ≥99.5%) as the electrodes under a pressure of 200 MPa. Chemical stability of the SEs towards Na metal was studied by monitoring the impedance change vs. time of the symmetric cell Na|SE|Na, which was assembled by attaching two same pieces of Na metal foils (~100 μm in thickness) on both sides of the SEs. For the

fabrication of tri-layer electrolytes, ~150 mg of Na₃PS_{3.85}O_{0.15} glass or Na₃PS₄ glass-ceramic SE powders were cold-pressed at 75 MPa; then ~25 mg of Na₃PS_{3.4}O_{0.6} glass powders were evenly distributed on both sides of as-pressed pellet; finally the three layers were co-pressed at 450 MPa. Following the attachment of Na metal foils to the tri-layer electrolyte, a Na plating/stripping test was performed in galvanostatic mode with an initial stacking pressure of 7 MPa.

Since Na₃PS_{3.85}O_{0.15} is the most conductive among the NPSO SEs and Ketjen black carbon (surface area of 1400 m² g⁻¹), they were chosen to blend with sulfur to create both fast ionic and electronic pathways for the sulfur active material in the composite cathode. The all-solid-state Na metal-sulfur batteries were fabricated using a Na₃PS_{3.85}O_{0.15}|Na₃PS_{3.4}O_{0.6} bi-layer electrolyte, sulfur-Ketjen black-Na₃PS_{3.85}O_{0.15} composite, and Na metal as the separator, cathode, and anode, respectively. In detail, sulfur (99.5%, Alfa Aesar) and Ketjen black (EC-600JD, AkzoNobel) powders with a weight ratio of 1:1 were ball-milled in an agate jar at a rotation speed of 500 rpm for 20 h to obtain a sulfur/KB nanocomposite, which was then milled with Na₃PS_{3.85}O_{0.15} powders at a rotation speed of 350 rpm for 30 min. The weight ratio of sulfur: KB: Na₃PS_{3.85}O_{0.15} composite cathode is 2:2:6. 150 mg Na₃PS_{3.85}O_{0.15} electrolyte powders were firstly pressed at 75 MPa into a pellet, of which one side was then uniformly covered with 20 mg Na₃PS_{3.4}O_{0.6} powders and ~1 mg composite cathode powders. Bulk-type all-solid-state Na-S batteries were fabricated after copressing at 450 MPa and attaching a piece of Na metal foil. Galvanostatic tests were performed in the potential range of 1.0 to 3.0 V vs. Na at different current densities from 0.05 to 0.35 mA cm $^{-2}$. All the electrochemical tests were conducted at 60 °C except where otherwise stated.

Data availability

The data that support the plots within this paper and other findings are available from the corresponding authors upon reasonable request.

References

- Dunn, B., Kamath, H. & Tarascon, J.-M. Electrical Energy Storage for the Grid: A Battery of Choices. *Science* **334**, 928-935, (2011).
- 2 Tarascon, J. M. & Armand, M. Issues and challenges facing rechargeable lithium batteries. *Nature* **414**, 359, (2001).
- Janek, J. & Zeier, W. G. A solid future for battery development. *Nat. Energy* 1, 16141, (2016).
- 4 Zhao, C. et al. Solid-State Sodium Batteries. Adv. Energy Mater. 0, 1703012, (2018).
- 5 Zhang, Z. *et al.* New horizons for inorganic solid state ion conductors. *Energy Environ. Sci* **11**, 1945-1976, (2018).
- Wen, Z., Hu, Y., Wu, X., Han, J. & Gu, Z. Main Challenges for High Performance NAS Battery: Materials and Interfaces. *Adv. Funct. Mater.* **23**, 1005-1018, (2013).
- Wang, Y. X. *et al.* Room-Temperature Sodium-Sulfur Batteries: A Comprehensive Review on Research Progress and Cell Chemistry. *Adv. Energy Mater.* 7, 1602829, (2017).
- 8 Kim, S. M. *et al.* Influence of Carbon Coating on Beta-Alumina Membrane for Sodium-Nickel Chloride Battery. *Bull. Korean Chem. Soc.* **36**, 2869-2874, (2015).
- Zhou, W., Li, Y., Xin, S. & Goodenough, J. B. Rechargeable Sodium All-Solid-State Battery. *ACS Cent. Sci.* **3**, 52-57, (2017).
- Nikolaev, Y. V., Vybyvanets, V. I., Belousenko, A. P., Dzalandinov, D. N. & Fedorova, V. N. in *IECEC 96. Proceedings of the 31st Intersociety Energy Conversion Engineering Conference.* 1191-1194 vol.1192.
- Porz, L. *et al.* Mechanism of Lithium Metal Penetration through Inorganic Solid Electrolytes. *Adv. Energy Mater.* **7**, 1701003, (2017).
- Tian, Y. *et al.* Compatibility issues between electrodes and electrolytes in solid-state batteries. *Energy Environ. Sci* **10**, 1150-1166, (2017).
- Wenzel, S. *et al.* Interfacial Reactivity Benchmarking of the Sodium Ion Conductors Na3PS4 and Sodium β-Alumina for Protected Sodium Metal Anodes and Sodium All-Solid-State Batteries. *ACS Appl. Mater. Interfaces* **8**, 28216-28224, (2016).
- Wu, E. A. *et al.* New Insights into the Interphase between the Na Metal Anode and Sulfide Solid-State Electrolytes: A Joint Experimental and Computational Study. *ACS Appl. Mater. Interfaces* **10**, 10076-10086, (2018).
- Tang, H. *et al.* Probing Solid-Solid Interfacial Reactions in All-Solid-State Sodium-Ion Batteries with First-Principles Calculations. *Chem. Mater.* **30**, 163-173, (2018).
- Lazar, M., Kmiec, S., Joyce, A. & Martin, S. W. Investigations into Reactions between Sodium Metal and Na3PS4–xOx Solid-State Electrolytes: Enhanced Stability of the Na3PS3O Solid-State Electrolyte. *ACS Appl. Energy Mater.* **3**, 11559-11569, (2020).
- Hudgens, J. J. & Martin, S. W. Glass Transition and Infrared Spectra of Low-Alkali, Anhydrous Lithium Phosphate Glasses. *J. Am. Ceram. Soc.* **76**, 1691-1696, (1993).

- Nose, M., Kato, A., Sakuda, A., Hayashi, A. & Tatsumisago, M. Evaluation of mechanical properties of Na2S-P2S5 sulfide glass electrolytes. *J. Mater. Chem. A* **3**, 22061-22065, (2015).
- Holzwarth, N. A. W., Lepley, N. D. & Du, Y. A. Computer modeling of lithium phosphate and thiophosphate electrolyte materials. *J. Power Sources* **196**, 6870-6876, (2011).
- Zhu, Y., He, X. & Mo, Y. Origin of Outstanding Stability in the Lithium Solid Electrolyte Materials: Insights from Thermodynamic Analyses Based on First-Principles Calculations. *ACS Appl. Mater. Interfaces* 7, 23685-23693, (2015).
- Han, F., Zhu, Y., He, X., Mo, Y. & Wang, C. Electrochemical Stability of Li10GeP2S12 and Li7La3Zr2O12 Solid Electrolytes. *Adv. Energy Mater.* **6**, 1501590, (2016).
- Berbano, S. S., Seo, I., Bischoff, C. M., Schuller, K. E. & Martin, S. W. Formation and structure of Na2S+P2S5 amorphous materials prepared by melt-quenching and mechanical milling. *J. Non-Cryst. Solids* **358**, 93-98, (2012).
- Dive, A., Zhang, Y., Yao, Y., Martin, S. W. & Banerjee, S. Investigations of the structure of Na2S + P2S5 glassy electrolytes and its impact on Na+ ionic conductivity through ab initio molecular dynamics. *Solid State Ion.* **338**, 177-184, (2019).
- Bischoff, C., Schuller, K., Dunlap, N. & Martin, S. W. IR, Raman, and NMR Studies of the Short-Range Structures of 0.5Na2S + 0.5[xGeS2 + (1–x)PS5/2] Mixed Glass-Former Glasses. *J. Phys. Chem. B* **118**, 1943-1953, (2014).
- Hayashi, A., Noi, K., Sakuda, A. & Tatsumisago, M. Superionic glass-ceramic electrolytes for room-temperature rechargeable sodium batteries. *Nat. Commun.* **3**, 856, (2012).
- Yu, Z. *et al.* Exceptionally High Ionic Conductivity in Na3P0.62As0.38S4 with Improved Moisture Stability for Solid-State Sodium-Ion Batteries. *Adv. Mater.* **29**, 1605561, (2017).
- 27 Chu, I.-H. *et al.* Room-Temperature All-solid-state Rechargeable Sodium-ion Batteries with a Cl-doped Na3PS4 Superionic Conductor. *Sci. Rep.* **6**, 33733, (2016).
- 28 Kim, Y., Saienga, J. & Martin, S. W. Anomalous Ionic Conductivity Increase in Li2S + GeS2 + GeO2 Glasses. *J. Phys. Chem. B* **110**, 16318-16325, (2006).
- Minami, K., Mizuno, F., Hayashi, A. & Tatsumisago, M. Structure and properties of the 70Li2S·(30-x)P2S5·xP2O5 oxysulfide glasses and glass-ceramics. *J. Non-Cryst. Solids* **354**, 370-373, (2008).
- Noi, K., Hayashi, A. & Tatsumisago, M. Structure and properties of the Na2S-P2S5 glasses and glass-ceramics prepared by mechanical milling. *J. Power Sources* **269**, 260-265, (2014).
- Hayashi, A., Noi, K., Tanibata, N., Nagao, M. & Tatsumisago, M. High sodium ion conductivity of glass–ceramic electrolytes with cubic Na3PS4. *J. Power Sources* **258**, 420-423, (2014).
- Tsukasaki, H., Mori, S., Morimoto, H., Hayashi, A. & Tatsumisago, M. Direct observation of a non-crystalline state of Li2S–P2S5 solid electrolytes. *Sci. Rep.* **7**, 4142, (2017).
- Jha, P. K., Pandey, O. P. & Singh, K. Structural and thermal properties of Na2S-P2S5 glass and glass ceramics. *J. Non-Cryst. Solids* **379**, 89-94, (2013).
- Hirai, K., Tatsumisago, M., Takahashi, M. & Minami, T. 29Si and 31P MAS-NMR Spectra of Li2S-SiS2-Li3PO4 Rapidly Quenched Glasses. *J. Am. Ceram. Soc.* **79**, 349-352, (1996).
- Kmiec, S., Joyce, A. & Martin, S. W. Glass formation and structural analysis of Na4P2S7-xOx, 0≤x≤7 sodium oxy-thiophosphate glasses. *J. Non-Cryst. Solids* **498**, 177-189, (2018).

- Tan, G., Wu, F., Li, L., Liu, Y. & Chen, R. Magnetron Sputtering Preparation of Nitrogen-Incorporated Lithium-Aluminum-Titanium Phosphate Based Thin Film Electrolytes for All-Solid-State Lithium Ion Batteries. *J. Phys. Chem. C* **116**, 3817-3826, (2012).
- Jha, P. K., Pandey, O. P. & Singh, K. FTIR spectral analysis and mechanical properties of sodium phosphate glass-ceramics. *J. Mol. Struct.* **1083**, 278-285, (2015).
- Hayashi, A., Tatsumisago, M., Minami, T. & Miura, Y. Structural Investigation of 95(0.6Li2S0.4SiS2)5Li4SiO4 Oxysulfide Glass by Using X-ray Photoelectron Spectroscopy. *J. Am. Ceram. Soc.* **81**, 1305-1309, (1998).
- Nesbitt, H. W. *et al.* Bridging, non-bridging and free (O2–) oxygen in Na2O-SiO2 glasses: An X-ray Photoelectron Spectroscopic (XPS) and Nuclear Magnetic Resonance (NMR) study. *J. Non-Cryst. Solids* **357**, 170-180, (2011).
- Kim, Y., Saienga, J. & Martin, S. W. Glass formation in and structural investigation of Li2S+GeS2+GeO2 composition using Raman and IR spectroscopy. *J. Non-Cryst. Solids* **351**, 3716-3724, (2005).
- Hayashi, A., Tanihata, N. & Tatsumisago, M. Development of all solid sodium-sulfur based battery with high capacity using electrolytes containing sulfur compounds. *Electrochemistry (Tokyo, Jpn.)* **82**, 175-180, (2014).
- Liu, H. *et al.* Controlling Dendrite Growth in Solid-State Electrolytes. *ACS Energy Lett.* **5**, 833-843, (2020).
- Ren, Y., Shen, Y., Lin, Y. & Nan, C.-W. Direct observation of lithium dendrites inside garnet-type lithium-ion solid electrolyte. *Electrochem. Commun.* **57**, 27-30, (2015).
- Cheng, E. J., Sharafi, A. & Sakamoto, J. Intergranular Li metal propagation through polycrystalline Li6.25Al0.25La3Zr2O12 ceramic electrolyte. *Electrochim. Acta* **223**, 85-91, (2017).
- 45 Xu, R., Sun, H., de Vasconcelos, L. S. & Zhao, K. Mechanical and Structural Degradation of LiNixMnyCozO2 Cathode in Li-Ion Batteries: An Experimental Study. *J. Electrochem. Soc.* **164**, A3333-A3341, (2017).
- Field, J. S., Swain, M. V. & Dukino, R. D. Determination of fracture toughness from the extra penetration produced by indentation-induced pop-in. *J. Mater. Res.* **18**, 1412-1419, (2003).
- 47 McGrogan, F. P. *et al.* Compliant Yet Brittle Mechanical Behavior of Li2S-P2S5 Lithium-Ion-Conducting Solid Electrolyte. *Adv. Energy Mater.* **7**, 1602011, (2017).
- 48 Kato, A., Yamamoto, M., Sakuda, A., Hayashi, A. & Tatsumisago, M. Mechanical Properties of Li2S–P2S5 Glasses with Lithium Halides and Application in All-Solid-State Batteries. *ACS Appl. Energy Mater.* 1, 1002-1007, (2018).
- Sakuda, A., Hayashi, A., Takigawa, Y., Higashi, K. & Tatsumisago, M. Evaluation of elastic modulus of Li2S-P2S5 glassy solid electrolyte by ultrasonic sound velocity measurement and compression test. *J. Ceram. Soc. Jpn.* **121**, 946-949, (2013).
- Monroe, C. & Newman, J. The Impact of Elastic Deformation on Deposition Kinetics at Lithium/Polymer Interfaces. *J. Electrochem. Soc.* **152**, A396-A404, (2005).
- Bonanos, N., Steele, B. C. H. & Butler, E. P. in *Impedance Spectroscopy* 205-537 (John Wiley & Sons: Hoboken, 2005).
- Irvine, J. T. S., Sinclair, D. C. & West, A. R. Electroceramics: Characterization by Impedance Spectroscopy. *Adv. Mater.* **2**, 132-138, (1990).
- Foulger, S. H. in 1998 Annual Report Conference on Electrical Insulation and Dielectric Phenomena (Cat. No.98CH36257). 282-287 vol. 281.

- Han, F. *et al.* High electronic conductivity as the origin of lithium dendrite formation within solid electrolytes. *Nat. Energy* **4**, 187-196, (2019).
- Tian, H.-K., Liu, Z., Ji, Y., Chen, L.-Q. & Qi, Y. Interfacial Electronic Properties Dictate Li Dendrite Growth in Solid Electrolytes. *Chem. Mater.* **31**, 7351-7359, (2019).
- Tsai, C.-L. *et al.* Dendrite-tolerant all-solid-state sodium batteries and an important mechanism of metal self-diffusion. *J. Power Sources* **476**, 228666, (2020).
- 57 Chi, X. *et al.* Tailored Organic Electrode Material Compatible with Sulfide Electrolyte for Stable All-Solid-State Sodium Batteries. *Angew. Chem. Int. Ed.* **57**, 2630-2634, (2018).
- Lu, X., Xia, G., Lemmon, J. P. & Yang, Z. Advanced materials for sodium-beta alumina batteries: Status, challenges and perspectives. *J. Power Sources* **195**, 2431-2442, (2010).
- 59 Song, S., Duong, H. M., Korsunsky, A. M., Hu, N. & Lu, L. A Na+ Superionic Conductor for Room-Temperature Sodium Batteries. *Sci. Rep.* **6**, 32330, (2016).
- Park, C.-W. *et al.* Discharge properties of all-solid sodium-sulfur battery using poly(ethylene oxide) electrolyte. *J. Power Sources* **165**, 450-454, (2007).
- Zhu, T. *et al.* An All-Solid-State Sodium-Sulfur Battery Using a Sulfur/Carbonized Polyacrylonitrile Composite Cathode. *ACS Appl. Energy Mater.* **2**, 5263-5271, (2019).
- Nagata, H. & Chikusa, Y. An All-solid-state Sodium-Sulfur Battery Operating at Room Temperature Using a High-sulfur-content Positive Composite Electrode. *Chem. Lett.* **43**, 1333-1334, (2014).
- Tanibata, N., Deguchi, M., Hayashi, A. & Tatsumisago, M. All-Solid-State Na/S Batteries with a Na3PS4 Electrolyte Operating at Room Temperature. *Chem. Mater.* **29**, 5232-5238, (2017).
- Yue, J. *et al.* High-Performance All-Inorganic Solid-State Sodium–Sulfur Battery. *ACS Nano* **11**, 4885-4891, (2017).
- Fan, X. *et al.* High-Performance All-Solid-State Na–S Battery Enabled by Casting–Annealing Technology. *ACS Nano* **12**, 3360-3368, (2018).
- Ando, T., Sakuda, A., Tatsumisago, M. & Hayashi, A. All-solid-state sodium-sulfur battery showing full capacity with activated carbon MSP20-sulfur-Na3SbS4 composite. *Electrochem. Commun.* **116**, 106741, (2020).

Acknowledgements

Y.Y. and S.W.M. gratefully acknowledge funding from the United States Department of Energy's Advanced Research Projects Agency-Energy (ARPA-E) (Award number DE-AR0000654). X.C. thanks the National Natural Science Foundation of China for its support (No. 51901240). Y.Y. also thanks the Research Corporation of Science Advancement (# 27110) for its support with Scialog: Advanced Energy Storage collaboration award. This research used resources of the Advanced Photon Source, a U.S. Department of Energy (DOE) Office of Science User Facility operated for the DOE Office of Science by Argonne National Laboratory under Contract No. DE-

AC02-06CH11357. ToF-SIMS analysis was carried out with support provided by the National Science Foundation CBET-1626418. This work was conducted in part using resources of the Shared Equipment Authority at Rice University.

Author contributions

X.C., S.W.M, and Y.Y. proposed the research. X.C. synthesized the materials, assembled the batteries, and performed the electrochemical characterizations. Y.Z. and L.W. carried out the lab-based XRD and synchrotron XRD measurements. S.K. and Y.Z. performed the Raman, NMR, FTIR and DSC measurements. F.H., H.D. conducted XPS characterizations and spectra fitting. K.Z. and R.X. designed and performed the mechanical measurements. L.Z. and L.G. repeated the NPSO synthesis and electrochemical tests. Q.A., T.T., and J.L. performed TOF-SIMS measurements. H.X. conducted TEM measurement. X.C., Y.Z., and F.H. co-wrote the first draft with inputs from all other co-authors. S.W.M, S.K., and Y.Y. revised and finalized the manuscript.

Conflict of Interests

Y.Y. and X.C. filed a US Patent Application 202106678A. Y.Y. has equity interest in LiBeyond LLC. His relationship with LiBeyond LLC has been reviewed and approved by the University of Houston in accordance with its conflict of interest policies. The remaining authors declare no competing interests.